Available online at www.sciencedirect.com
SCIENCE DIRECT®
International Journal of Heat and Fluid Flow 25 (2004) 581–592
International Journal of HEAT AND FLUID FLOW
www.elsevier.com/locate/ijhff

Large eddy simulation of periodically perturbed separated flow over a backward-facing step

A. Dejoan, M.A. Leschziner *

Department of Aeronautics, Imperial College, Prince Consort Road, London, SW7 2AZ, UK

Received 9 September 2003; accepted 24 March 2004
Available online 7 June 2004

Abstract

Large eddy simulation is used to investigate the effects of a periodic perturbation introduced into a separated shear layer that borders a recirculation bubble behind a backward-facing step in a high-aspect-ratio channel. The perturbation is provoked by the injection of a slot jet, at zero net mass-flow rate, uniformly along the spanwise edge at which separation occurs. Attention is focused on one particular jet-forcing frequency, at the Strouhal number 0.2, for which experimental data show the perturbation to cause a maximum change to the properties of the unperturbed flow – in particular, the largest reduction in the time-mean recirculation length. Results are reported for time-mean and phase-averaged velocity and Reynolds stresses, and these are compared with experimental data. The time evolution of phase-averaged properties, including stream-function, pressure and turbulence energy, are investigated in an effort to identify the mechanisms responsible for the observed substantial changes to the time-mean properties. This is aided by a study of some spectral properties. The simulations are shown to reproduce the experimental observations, and these provide clear indications that the high level of sensitivity to the perturbation at the Strouhal number considered is due to a strong interaction between shear-layer instabilities, which are amplified by the perturbation, and shedding-type instabilities, which are induced by the interaction of large-scale structures developing downstream of the step with the wall, causing the shear-layer to flap.

Keywords: Large eddy simulation; Turbulent recirculating flow; Backward-facing step; Separation control; Unsteady flow

1. Introduction

The control of turbulent flows by external forcing, either steady or unsteady, is of much practical as well as fundamental interest. Methods of flow control in a practical context include skin-friction reduction by means of grooves and compliant surfaces, separation control on aircraft wings by means of solid vortex generators and jets, the use of lobbed and serrated mixers in jet-engine exhausts to promote mixing and reduce noise, and the suppression of shedding from cylindrical bodies and blunt trailing edges of turbomachine blades by local blowing or the addition of geometric features such as dimples, bulges, serrations and spanwise fins.

The fundamental mechanisms underlying the response of a flow to a controlling agency are as varied as the nature of the forcing, the type and scales of the phenomena to be controlled and the practical circumstances. At the small-scale end of the range, surface-drag reduction by sub-boundary-layer features (of size $y^+ = \mathrm{O}(10)$) or transpiration appears to be effected by a modification of the structure of the near-wall streaks and their distance to the wall. At the much more *energetic* end of the range, strong jets, either steady or pulsating, are injected into a baseline flow in order to introduce streamwise vorticity and to promote mixing across the entire boundary layer, often with the objective of preventing separation under the influence of an adverse pressure gradient or of reducing the size of the separation zone. The present paper is concerned with the latter – specifically the control of reattachment and thus

* Corresponding author. Tel.: +44-20-759-45061; fax: +44-20-758-48120.
E-mail addresses: a.dejoan@imperial.ac.uk (A. Dejoan), mike.leschziner@imperial.ac.uk (M.A. Leschziner).
URL: http://www.ae.ic.ac.uk/research/tfms/index.html.

0142-727X/$ - see front matter © 2004 Elsevier Inc. All rights reserved.
doi:10.1016/j.ijheatfluidflow.2004.03.004

the reduction in the size and intensity of the separated zone by means of an oscillatory disturbance introduced into the separated shear layer.

Investigations into the control of separation bubbles along a blunt circular cylinder with a square leading edge (Sigurdson, 1995; Kiya et al., 1997), as well as of backward-facing-step flow (Hasan, 1992), suggest that both a shear-layer instability and a shedding-type instability are involved in the promotion of reattachment. The former instability mode corresponds to the natural roll-up process of the shear layer and the latter to the interaction of the entire shear layer with the wall. The shedding instability is directly related to the large vortical structures which impinge onto the wall and induce a 'flapping' motion characterized by a lower frequency than that of the shear-layer mode. The role of the shear layer is seen as a potential 'amplifier' of the forcing: if the disturbance can be amplified by the shear layer, the large vortical structures grow faster and interact earlier with the wall, thus promoting reattachment.

The present study focuses on the control of a separated flow by the pulsed injection of a jet into a separating shear layer behind a backward-facing step. The study was motivated by experimental investigations by Chun and Sung (1996, 1998) and especially Yoshioka et al. (2001a,b). In both cases, the 'jet' is a combination of alternate periods of blowing and suction. The paper presents LES results corresponding to the conditions of the latter study. The authors are aware of only one simulation of this type of flow by Wengle et al. (2001), but this was for a transitional flow at different conditions.

The gross effect observed experimentally in response to the injection is a significant shortening of the time-averaged recirculation zone. The primary mechanism at play, revealed by phase-averaged velocity fields, is the formation of large-scale unsteady vortices in the recirculation zone, associated with 'flapping'. These generate high rates of strain between vortices, thus enhancing turbulence generation and momentum transport (in a statistical sense). The fact that the degree of shortening is observed to be quite sensitive to the frequency of injection, with the optimum value lying within a narrow range, suggests that the forcing is most effectively amplified at this frequency due to the interaction of the shear-layer instability with the shedding instability highlighted in the previous paragraph. Secondary mechanisms could include an influence on the spanwise coherence of vortices in the shear layer and thus on their three-dimensional (3D, henceforth) breakdown. From a statistical perspective, the introduction of energy at a particular frequency may influence the energy transfer between scales, thus modifying the rate at which vortices break down towards the dissipative range of scales. These mechanisms are clearly of interest from a fundamental point of view. They may also have wider applicability to turbulent flows affected by unsteady perturbations – for example, in the context of wake-blade interaction in turbomachinery, flutter, buffet and buzz in aerodynamic flows and flow-induced vibrations in slender cylindrical bodies.

The measurements to which the present LES solutions correspond were undertaken with two-dimensional (2D, henceforth) PIV in a channel of aspect ratio 12 at Reynolds numbers of 1800–5500, based on the centre-line velocity in the channel upstream of the step and the step height. For all Reynolds numbers, and in agreement with the results of Chun and Sung, Yoshioka et al. observed a distinct minimum in the recirculation length at the Strouhal number $St = 0.2$, with the reduction in length being of order 30%. This is the reason for the present focus on the value 0.2. The fact that Yoshioka et al.'s flow is close to being statistically spanwise homogeneous and the relatively low value of the Reynolds number provide strong incentives to undertake highly-resolved large eddy simulations of that flow and study the fundamentals of the pulsed-jet/shear-layer interaction. While the PIV data yielded a wealth of information on the phase-averaged velocity and second moments, a simulation provides a greater level of detail, allowing a wider range of fundamental issues to be studied. Moreover, a simulation can be arranged to secure essentially perfect spanwise homogeneity and hence freedom from 3D contamination. Because of this contamination, unavoidable in the experiment, the unperturbed flow, used as the reference case, also needed to be simulated, in order to create a valid background against which the effects of the forcing could be quantified. The simulation of the unperturbed case has also offered the opportunity to extract data from which budgets for the Reynolds stresses have been evaluated. Some of these are given in the present paper, while a more extensive exposition is given elsewhere. Although several simulations for unperturbed backward-facing step flows have been published, the latest by Le et al. (1997), limited information has been provided on second-moment budgets.

2. The simulated flow conditions

The geometry of the flow simulated is shown in Fig. 1. The inlet stream, at $Re = 3700$ (based on maxi-

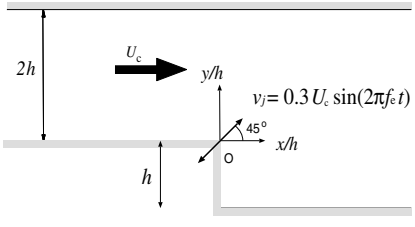

Fig. 1. Backward-facing-step flow.

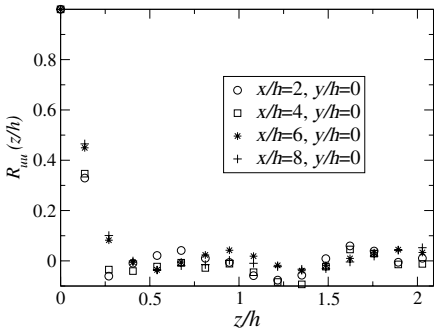

Fig. 2. Auto-correlation coefficient in the spanwise direction at different streamwise locations; unperturbed flow.

mum inlet velocity U_c and step height h), is turbulent and fully developed at the step. In the experiment, the channel downstream of the step is $50h$ long in the streamwise direction, and the aspect ratio, based on h and the channel span, is 1:12. The channel-expansion ratio is 1.5. In the simulation, the spanwise direction was treated as statistically homogeneous, with periodic conditions prescribed at the spanwise boundaries of the computational box. From the step, the box extends to $12h$ in the streamwise direction and has a depth of $4\pi h/3$ in the spanwise direction. Fig. 2 shows distributions of the auto-correlation coefficient R_{uu} along several spanwise lines at different streamwise locations within the separated shear layer. As can be seen, the spanwise extent is sufficient to ensure spanwise decorrelation.

Two flows were simulated, one without injection and the other with a slot jet that is injected at the step at 45° into the flow across the entire span through a 1 mm slit at a velocity

$$v_j = 0.3U_c \sin(2\pi f_e t) \tag{1}$$

where U_c is the maximum streamwise velocity in the channel ahead of the step. In the experiment, the amplitude was chosen on the basis of the observation that larger values did not result in a further reduction in the mean reattachment distance, thus being practically ineffective.

The inlet conditions were generated by a pre-cursor simulation for a fully developed channel flow in a periodic domain of length $4h$ at the appropriate Reynolds number. The conditions were then prescribed at $x/h = -4$ by feeding in realisations of the cross-sectional conditions from a data file, with the cross-sectional fields chosen subject to the Taylor hypothesis. At the outlet, the convective condition

$$\frac{\partial U_i}{\partial t} + \overline{U}\frac{\partial U_i}{\partial x} = 0 \tag{2}$$

was imposed, in which $\overline{U}$ is the average outlet-channel velocity.

3. The computational procedure and the mesh

The computational scheme is a general multiblock finite-volume procedure with non-orthogonal-mesh capabilities (Lardat and Leschziner, 1998). In the present case, a two-block rectilinear-mesh system was used, with one block covering the upstream channel and the other the downstream channel. The finite-volume scheme is second-order accurate in space, using central differencing for advection and diffusion. Time-marching is based on a fractional-step method, with the time derivative being discretised by a second-order backward-biased approximation. The flux terms are advanced explicitly using the Adams–Bashforth method. The provisional velocity field is then corrected via the pressure gradient by a projection onto a divergence-free velocity field. To this end, the pressure is computed as a solution to the pressure-Poisson problem by means of a partial-diagonalisation technique (Schumann and Sweet, 1988) and a V-cycle multigrid algorithm operating in conjunction with a successive-line over-relaxation scheme. The code is fully parallelised and was run on a multi-processor Cray T3E computer.

The domain downstream of the step is covered by a mesh of $96\times80\times32$ cells. The inlet channel is covered by a separate mesh of $96\times40\times32$ cells. Thus the total number of cells is around 4×10^5. An especially fine grid is used in the step and injection region. The *maximum* value of y^+ at both lower and upper walls is 1.5, and the cell-aspect ratios are, typically, $\Delta y^+/\Delta x^+/\Delta z^+ = 1.5/28/20$ at the wall and 4.5/28/20 in the shear layer. The expansion ratio of the grid does not exceed 1.05. This grid is the outcome of precursor testing. Among a number of aspects considered was the level of the Kolmogorov length $\eta = (\nu^3/\epsilon)^{1/4}$ relative to $\Delta = (\Delta x\Delta y\Delta z)^{1/3}$. To determine this ratio, plotted in Fig. 3 along several constant x/h and y/h lines, the dissipation rate was obtained from the turbulence-energy budget. As seen, the ratio Δ/η is lower than 10. Hence, the cut-off lies close to the dissipative part of the wave-number

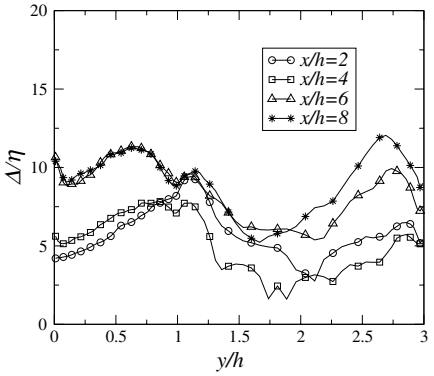

Fig. 3. Ratio of the cell size to the Kolmogorov scale along various grid lines; unperturbed flow.

range. As demonstrated by Fig. 18(d), showing a frequency spectrum of the streamwise stress at $x/h = 10$ and $y/h = 0$, the simulation resolves scales which span 2.5 decades.

Subgrid-scale processes were represented by means of either the Smagorinsky model (with van-Driest damping) or the WALE model (Ducros et al., 1998). Compared to the Smagorinsky model, the WALE model reproduces the cubic wall-asymptotic behaviour of the subgrid-scale viscosity and gives lower values of this viscosity (see Fig. 3 in Temmerman et al., 2003). However, as expected, in view of the above considerations on the choice of grid, there were insignificant differences between the statistical properties of the solutions, including the second moments. Akselvoll and Moin (1995) tested several subgrid-scale models, including the dynamic model, the localized dynamic model and the Smagorinsky model, in simulations of backward-facing-step flows at low and high Reynolds number on a relatively coarse mesh, and found that all the models gave very similar results when compared to DNS and experimental data. As the post-separation and reattachment processes are dominated by large-scale vortices, the influence of subgrid modelling is expected to be generally weak, provided the grid is reasonably fine.

4. Results for baseline flow

Selected statistical results for the unforced flow are contained in Figs. 4 and 5. To obtain these statistics, the solution was integrated over a total period $TU_c/h = 282$, which corresponds to 20 'flow-through' times. In addition, spanwise averaging was performed over the 32 spanwise planes.

The reattachment point, determined as the wall-nearest location at which the mean velocity changes sign, is predicted to be at $x_{r,o}/h = 7$. This value also

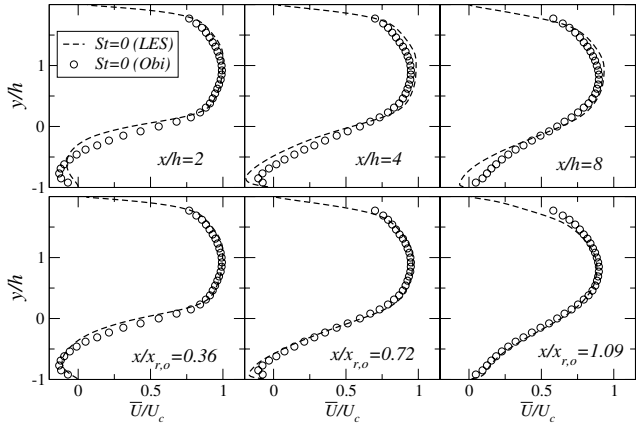

Fig. 4. Unperturbed flow: time-averaged streamwise velocity $\overline{U}/U_c$ at different streamwise locations x/h and $x/x_{r,o}$ downstream of the step.

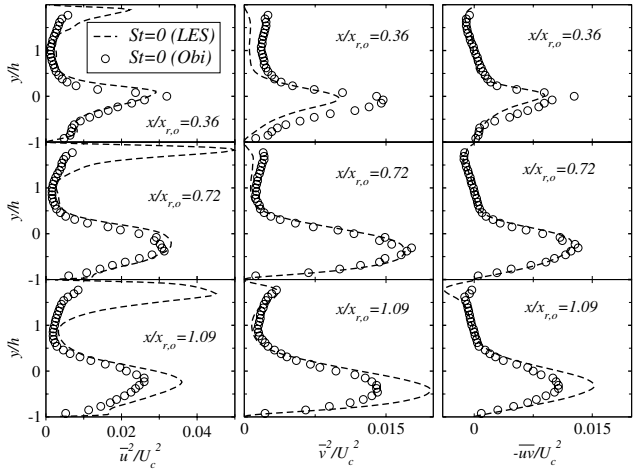

Fig. 5. Unperturbed flow: time-averaged Reynolds stresses at different streamwise locations $x/x_{r,o}$ downstream of the step.

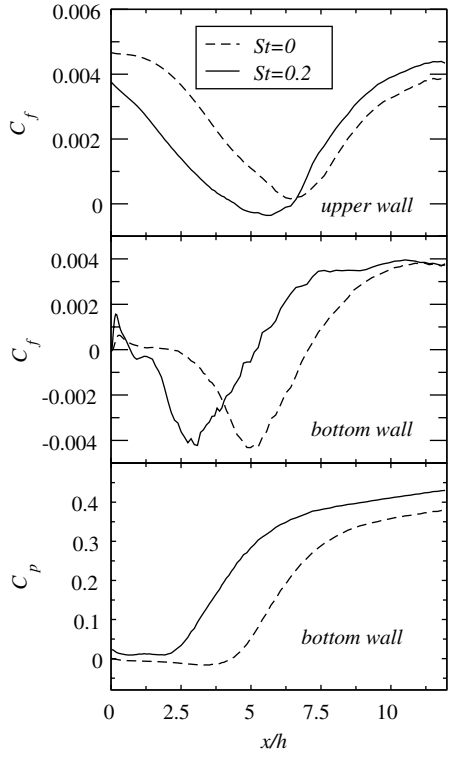

Fig. 6. Skin-friction coefficient, C_f, and step-wall pressure coefficient, C_p, in unperturbed and perturbed flows.

arises from the skin-friction plot for the lower wall in Fig. 6, which shows that a secondary vortex is predicted to nest in the step corner. Also noteworthy is the fact that the flow on the upper wall is close to separation (see Fig. 6). The predicted reattachment length is considerably larger than the experimental value 5.5. Experiments performed by Kasagi and Matsunaga (1995) at exactly the same expansion ratio, but at the somewhat higher Reynolds number of 5540, gave a value $x/h = 6.5$. As

the reattachment position tends to move upstream with increasing Reynolds number in the range $1200 < R_e < 6600$ (Armali et al., 1983), it appears that Yoshioka et al.'s value is an underestimate for purely 2D conditions, presumably reflecting 3D contamination. Further support is provided by the DNS data of Le et al. (1997) for $Re = 5100$, which gave reattachment at $x/h = 6.3$.

Two sets of streamwise-velocity profiles are given in Fig. 4. One set simply compares predicted and measured velocity values at the selected streamwise locations. In contrast, the other set compares each pair of profiles at identical values of *normalised* positions $x/x_{r,o}$, i.e. relative to the respective reattachment length. The latter presentation aims to compensate for 3D contamination and is based on the notion that the major component of this contamination is a global one, associated with the 3D conditions close to the spanwise walls causing a change in the pressure field, rather than local flow distortions in the spanwise direction. With this normalisation, there is close agreement between the predicted and the measured profiles.

Based on the above argument, second-moment profiles for $\overline{u^2}, \overline{v^2}$ and $\overline{uv}$ are plotted in Fig. 5 at fixed normalised positions. Although agreement between experiment and simulation is reasonably close in most respects, there are some substantial local discrepancies. Especially striking is the very high value of streamwise, i.e. stress, and hence anisotropy, predicted at the upper wall. In part, this reflects a lower resolution at the upper wall than at the lower wall, although there are five computational nodes within $y^+ = 20$. Test computations, performed for the unperturbed flow on a grid containing five times as many nodes as that used to generate the data reported herein, yielded a moderate reduction in the peak of $\overline{u^2}$ at the upper wall, although this peak is still higher than the maximum value in the separated shear layer. This behaviour is attributed to the fact that the flow at the upper wall, while just attached in the mean, features very large streamwise fluctuations associated with intermittent separation, with the instantaneous separation location moving rapidly over a substantial proportion of the wall. In the measurements, the flow does not appear to be as close to separation as is implied by the simulation. In any event, the emphasis of the study is on processes behind the step and their response to the perturbation, and these are largely insensitive to the details of the upper-wall boundary layer. Another point of difference arises from the somewhat higher level of anisotropy predicted close to the step, $x/x_{r,o} = 0.36$, although the shear-stress distributions are close. This may again reflect insufficient local resolution in the initial portion of separated shear layer, which is especially thin and highly strained. Excessive anisotropy in highly-sheared regions often betrays insufficient resolution.

For the present unperturbed case a wide range of further data have been extracted, including budgets for the second moments in which the pressure/velocity correlations terms have been decomposed into pressure diffusion and pressure–strain interaction. These results will be reported elsewhere.

5. Results for perturbed flow

5.1. Introductory comments

Results are presented below for the condition $St = 0.2$. As noted earlier, this frequency is observed to yield the largest effect on the time-mean fields. The simulation was started with a full 3D realisation of the unperturbed case. Following injection, the flow was then allowed to evolve towards a 'periodic' state within 15 injection periods, correspond to $TU_c/h = 79$. The simulation was then continued for a further 15 periods over which statistics were assembled. Especially in relation of phase-averaged results presented, it needs to be appreciated that the number of realisations contributing to the average value is low, namely 15×32. Thus, the distributions are not as smooth as might be desirable. However, this simulation is extremely costly, the number of realisations increasing only very slowly with the computational resource (i.e. by only 32 per injection period). The low sampling rate also applies, albeit to a much lesser extent, to the time-mean field. Here too, smoothness is affected detrimentally by the periodic nature of the flow, with the ratio $1/(f\Delta t)$ being around 2000.

5.2. Time-mean behaviour

As expected from the experimental observations, the computed reattachment length has been found to be substantially reduced by the perturbation. The predicted value is $\tilde{x}_r \equiv \tilde{x}_r/h = 5.5$, relative to 7 for the unperturbed case. Thus, the predicted reduction is 26%, a value that agrees well with the experimental finding of 30%. Fig. 6 compares the mean skin-friction distributions and pressure coefficients for the perturbed and unperturbed flows. These plots convey graphically the substantial effect of the injection. Because the recirculation region has been shortened, the rate of pressure recovery has increased, and this is seen to lead to incipient separation on the upper wall due to the increased adverse pressure gradient, while the unperturbed flow is still attached (in the mean).

Fig. 7 compares velocity profiles for the unperturbed and perturbed flows at specific normalised $x/x_{r,o}$ positions. The figure contains both the experimental and corresponding computational profiles. Agreement is seen to be close within the separated zone, and it may be

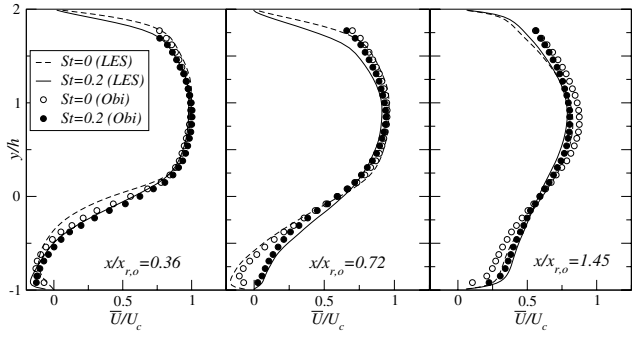

Fig. 7. Unperturbed and perturbed flows: time-averaged streamwise velocity $\overline{U}/U_c$ at different streamwise locations $x/x_{r,o}$ downstream of the step.

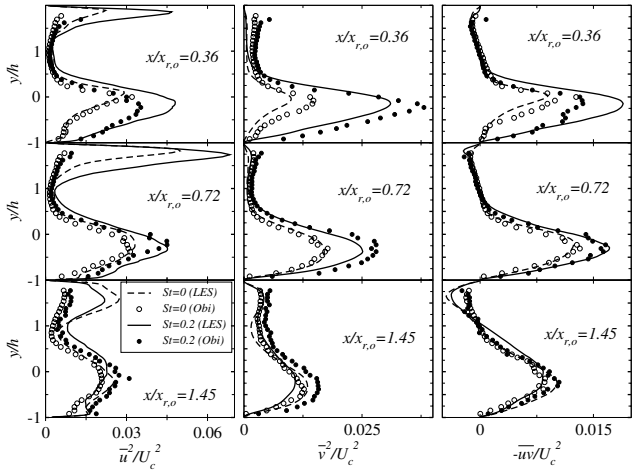

Fig. 8. Unperturbed and perturbed flows: time-averaged Reynolds stresses at different streamwise locations $x/x_{r,o}$ downstream of the step.

claimed, therefore, that the simulation has reproduced well the effect of the perturbation on the mean field. Beyond reattachment, the flow should recover progressively towards a fully-developed state. The velocity profiles at $x/x_{r,o} = 1.45$ show that the perturbation enhances the rate of recovery, although the simulation returns a somewhat weaker response than is suggested by the experiment.

Profiles of Reynolds stresses, corresponding to those for the velocity in Fig. 7, are shown in Fig. 8. The most striking feature is the major increase in turbulence activity provoked by the injection in the shear layer: close to the step, the lateral normal stress has increased by a factor 3, while the shear stress has risen by a factor 2. These increases are, qualitatively, consistent with the substantial reduction in recirculation length, as the injection provokes a much higher transport of momentum and hence more rapid recovery. Another striking feature is the substantial increase in the turbulence activity within the recirculation zone. As will emerge later, by reference to phase-averaged results, this is due to the formation of significant unsteady features below the shear layer associated with the 'flapping' of that layer.

A curious discrepancy between the simulated and the experimental behaviour of the stresses arises downstream, beyond the reattachment point. In the simulation, the transverse normal stress and the shear stress of the perturbed flow fall below those for the unperturbed case, while in the measurements the reverse occurs. Beyond reattachment, the flow recovers, and there should be an increasingly close correspondence between the shear strain and the shear stress. Reference to Fig. 7 shows that the shear strain in the near-wall wake region of the perturbed flow, at $x/x_{r,o} = 1.45$, is significantly smaller than that of the unperturbed flow. Hence, the expectation is that the shear stress should also be lower. This is indeed so in the simulation, but not in the experiment. The differences are caused by two effects: a more rapid streamwise reduction in the measured stresses relative to the simulation for the unperturbed case and the reverse in the perturbed case – or in other words, the recovery of the perturbed flow, in terms of the turbulence field, is predicted to be higher than that measured. It is relevant to add here that Chun and Sung observed in their experiments a faster post-reattachment recovery in their forced flow, relative to that in the corresponding unforced configuration, a behaviour in accord with the present LES results.

As indicated by experiments of Kasagi and Matsunaga (1995) for unperturbed conditions, the spanwise normal stress tends to be higher than the longitudinal component in the reattachment region. This is also observed here, both for the unperturbed and the perturbed flow, as shown in Fig. 9. Fig. 10 compares variations of the pressure–strain contributions to the streamwise and spanwise normal-stress budgets. These provide clear

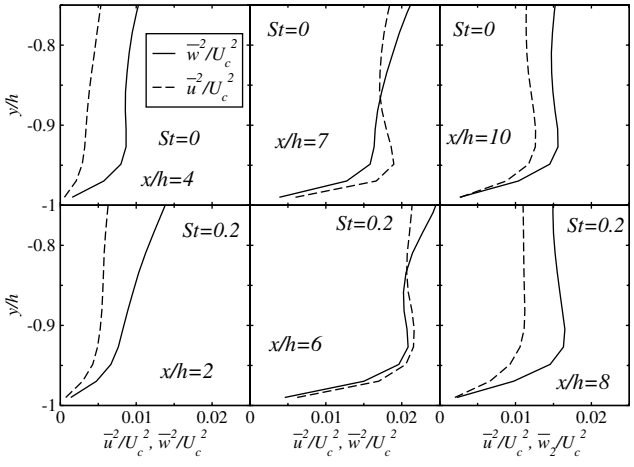

Fig. 9. Unperturbed and perturbed flows: time-averaged streamwise and spanwise normal stress $\overline{u}^2/U_c^2$, $\overline{w}^2/U_c^2$ in the reattachment region near the wall.

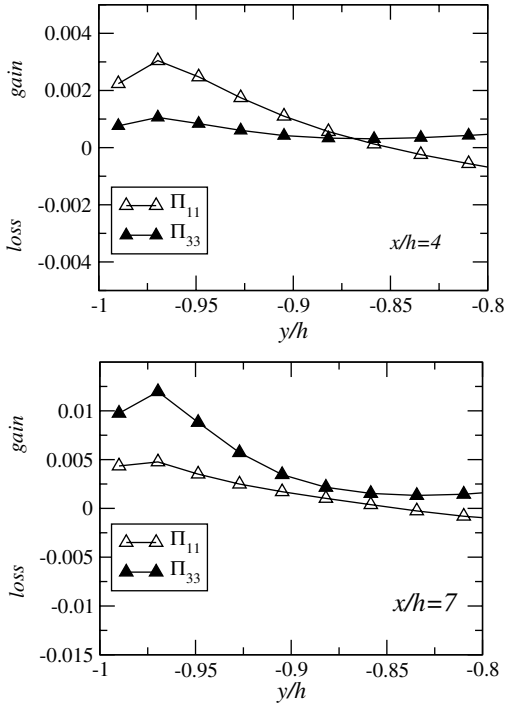

Fig. 10. Unperturbed flow: pressure–strain terms, Π_{11} and Π_{33} (see Eq. (5)), associated with the streamwise and spanwise normal stresses at different streamwise locations, normalized by U_c^3/h.

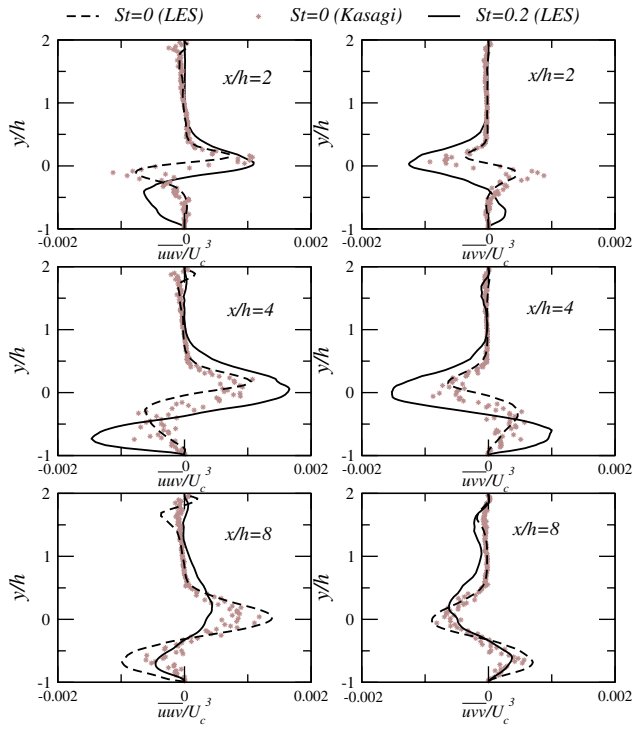

Fig. 11. Unperturbed and perturbed flows: time-averaged triple correlations associated with the shear stress $\overline{uv}/U_c^2$ at different streamwise locations downstream of the step.

evidence that the high level of spanwise fluctuations in this region is due to the pressure–strain interaction effecting a preferential transfer of turbulence energy from the streamwise to the spanwise direction by 'splatting'.

In reattaching flow, the turbulent diffusion of the Reynolds stresses contributes significantly to the budgets of the stresses. In the context of second moment closure, Parneix et al. (1998) have pointed out that the model for the triple correlations, representing turbulent diffusion, has a significant influence on the prediction of the stresses and thus on the momentum transfer. Fig. 11 provides comparisons of profiles for two triple correlations, $\overline{uuv}$ and $\overline{uvv}$, at three streamwise locations for both the unperturbed and perturbed flow, in comparison to experimental data by Kasagi and Matsunaga (1995) for unperturbed conditions. Although the Reynolds number of Kasagi and Matsunaga's flow is not the same as that of the present one, the distributions for both unperturbed flows agree well. Close to the step, the distributions are representative of those in a free shear layer. As the reattachment location is approached, the level of the triple correlations near the wall approaches that in the shear layer above it, thus rendering this process important in the balance of mechanisms affecting the stresses. When forcing is introduced, the predicted distribution suggests a substantial intensification of the turbulence–diffusion process before reattachment, consistent with a major increase in turbulence intensity in the recirculation region and the separated shear layer. It is noticeable that the profiles of the triple correlations exhibit a distinctly asymmetric shape close to the step (at $x/h = 2$), which suggests that the shear layer interacts earlier with the wall when the flow is forced. Well beyond reattachment, turbulence diffusion decays fairly rapidly, and this is consistent with the predicted higher rate of recovery induced by the injection, and a diminution of turbulence activity associated with the disturbance caused by the separation and reattachment processes.

5.3. Phase-averaged behaviour

The unsteadiness in the perturbed flow may be viewed as consisting of a stochastic component and a periodic component, the latter associated with the injection process. Thus, the instantaneous velocity may be represented by:

$$U_i = \overline{U}_i + \tilde{u}_i + u_i = \langle U_i \rangle + u_i \tag{3}$$

where U_i is the instantaneous velocity, $\overline{U_i}$ is the time-mean velocity and $\widetilde{u_i}$ is the periodic component; u_i denotes the turbulent component and $\langle U_i \rangle$ the phase-averaged component. To determine the phase-averaged component at any one phase location, ϕ, between 0 and 2π within the injection cycle, samples need to be taken (both experimentally and computationally) once every

cycle. Because the present simulation assumes a homogeneous spanwise coordinate, with 32 mesh planes covering the spanwise extent, 32 samples can be taken from the various planes at anyone phase position. Nevertheless, as pointed out earlier, the number of samples that could be generated was low, as only 15 injection periods were simulated. Thus, the following phase-averaged distributions are not claimed to be highly accurate. However, they do provide useful pointers to the mechanisms and processes associated with periodicity.

An overall view of the periodic behaviour is conveyed in Fig. 12, which shows contours of the phase-averaged velocity and pressure fluctuations at four phase locations separated by $\pi/2$. Both sets show that periodicity produces large-scale vortices below the separated shear layer. These are in good agreement with the experimental observations, which are not included here for space reasons. The structures move forward with a convective speed of $U_{cv} = 0.4U_c$, which compares with the experimental value $0.3U_c$. Beyond the reattachment point, no vortices appear to exist (although substracting from the phase-average velocity its time-averaged counterpart would reveal their persistence), and the only trace of the periodicity is the undulation of the streamlines. Again, this is in qualitative agreement with the experimental observations. The frictional footprint of the vortices on the lower wall emerges from Fig. 13, which shows the phase-averaged skin friction. Although the distributions are 'noisy', the existence of distinct peaks and troughs within the recirculation zone is recognised, and these coincide with large-scale positive and negative perturbations in the near-wall velocity associated with the vortices.

The overall picture thus presented is one in which the shear layer is 'flapping', a process related to the

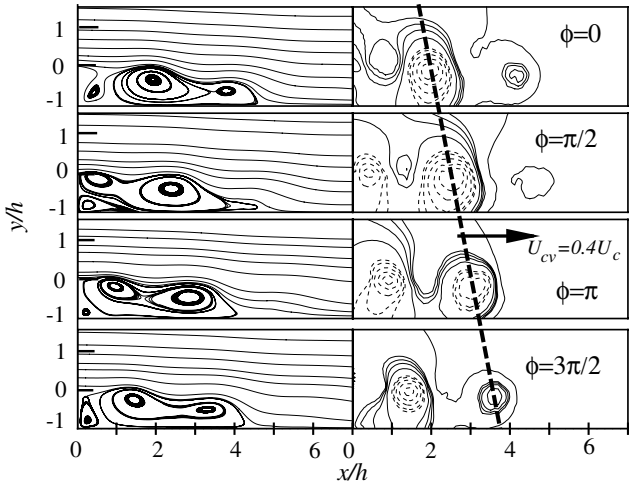

Fig. 12. Phase-averaged streamfunction and phase-averaged pressure fields in the reattachment region: negative pressure contours identified by dashed lines and positive pressure contours identified by solid lines.

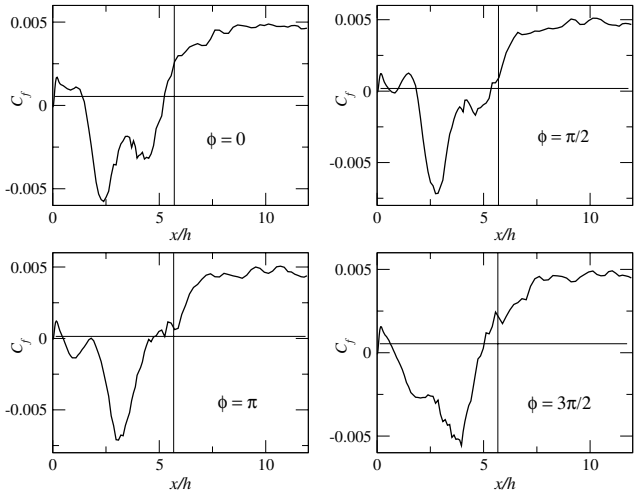

Fig. 13. Perturbed flow: phase-averaged skin-friction coefficient at the bottom-wall downstream the step.

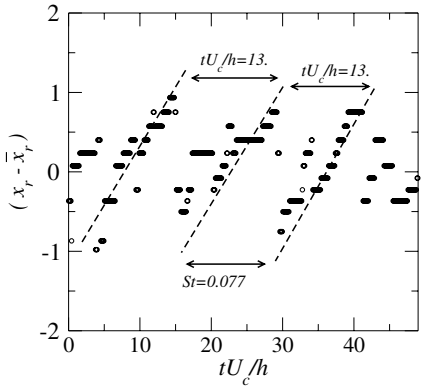

Fig. 14. Time-evolution of the spanwise-averaged instantaneous reattachment point.

interaction of the large-scale vortical structures with the wall around the reattachment zone. In this connection it is informative to consider Fig. 14, which shows a map of spanwise-averaged, instantaneous reattachment locations. This is also indicative of the flapping motion referred to above. Thus, the reattachment point shows a periodic behaviour closely tied to the passage of the large-scale structures depicted above, the reattachment length increasing and decreasing periodically. The period of this fluctuation corresponds to the time required for the large-scale vortices emerging from the step to travel downstream and to interact with the wall. Indeed, the convection velocity $U_{cv} = 0.4U_c$, and the average reattachment length, $\tilde{x}_r = 5.5$, combine to give $TU_c/h = 13.75$, which is close to the period $TU_c/h = 13$ extracted from Fig. 14. Expressed in terms of the Strouhal number, this period corresponds to the non-dimensional (low) frequency of the 'flapping' motion $St = 0.077$ mentioned earlier (more details are given in the next section). Fig. 14 also indicates that the periodic

rate of increase in the reattachment point is almost constant, at $d\tilde{x}_r/dt \sim 0.16$, and that the decrease occurs abruptly. This suggests that the large-scale structures remain in contact with the wall over some distance before suddenly detaching from the wall, causing the abrupt upstream shift of the reattachment line. This type of detachment of unsteady structures downstream of the reattachment region has been visualized by Hasan (1992).

The contours of the phase-averaged production rate of turbulence energy, $\langle P_k \rangle$, and of the Reynolds shear stress, $-\langle P_{12} \rangle$, are shown, alongside contours of the pressure–strain term for the shear stress $-\langle \Pi_{12} \rangle$, in Fig. 15. These terms constitute contributions to the budgets of the phase-averaged turbulence energy and Reynolds stresses, expressed by the respective transport equations:

$$\frac{\partial \langle k \rangle}{\partial t} + \underbrace{\langle U_j \rangle \langle k \rangle_{,j}}_{\langle C_k \rangle} = \underbrace{-\langle u_i u_j \rangle \langle U_{i,j} \rangle}_{\langle P_k \rangle} + \underbrace{\nu \langle k_{,jj} \rangle}_{\langle D_{\nu_k} \rangle} \underbrace{-\left\langle \left\langle u_j \frac{u_i u_i}{2} \right\rangle \right\rangle_{,j}}_{\langle TTT_k \rangle} \underbrace{-\left\langle \left\langle \frac{p}{\rho} u_j \right\rangle \right\rangle_{,j}}_{\langle \Pi_k \rangle} \underbrace{-\nu \langle u_{i,j} u_{i,j} \rangle}_{\langle \varepsilon \rangle} \tag{4}$$

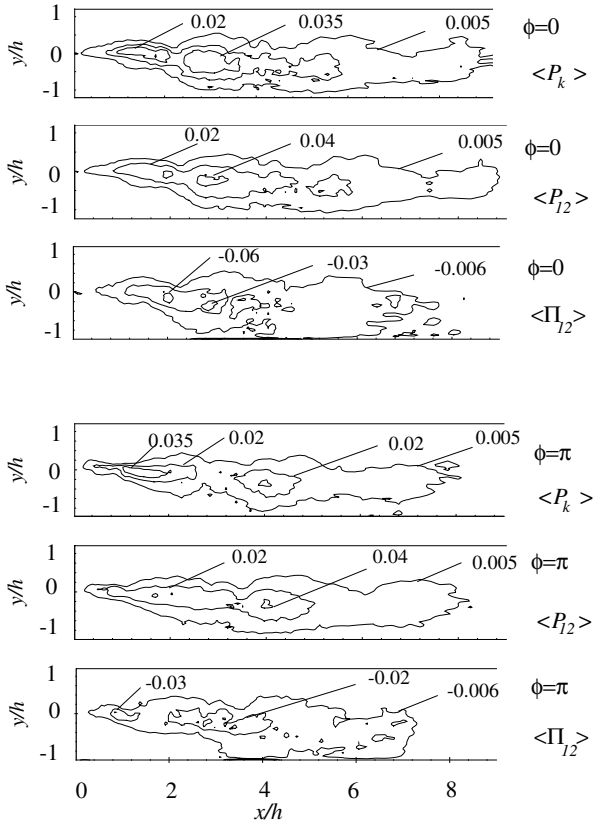

Fig. 15. Phase-averaged production rate of the turbulence energy, $\langle P_k \rangle$, of the production rate of the Reynolds shear stress, $\langle P_{uv} \rangle$, and phase-average of the pressure strain of the Reynolds shear stress, $\langle \Pi_{uv} \rangle$, normalized by U_c^3/h.

$$\frac{\partial \langle u_i u_j \rangle}{\partial t} + \underbrace{\langle U_k \rangle \langle u_i u_j \rangle_{,k}}_{\langle C_{ij} \rangle} = \underbrace{-\langle u_k u_j \rangle \langle U_{i,k} \rangle - \langle u_k u_i \rangle \langle U_{j,k} \rangle}_{\langle P_{ij} \rangle} + \underbrace{\nu \langle u_i u_j \rangle_{,kk}}_{\langle D_{f_{ij}} \rangle} \underbrace{-\langle u_i u_j u_k \rangle_{,k}}_{\langle TTT_{ij} \rangle} \underbrace{-\frac{\left(\langle u_j p_{,j} \rangle + \langle u_j p_{,i} \rangle \right)}{\rho}}_{\langle \Pi_{ij} \rangle} \underbrace{-2\nu \langle u_{i,k} u_{j,k} \rangle}_{\langle \varepsilon_{ij} \rangle} \tag{5}$$

Closer inspection of these fields, in comparison with the streamfunction fields in Fig. 12, reveals that turbulence-production maxima coincide with regions lying between vortices, while minima are roughly in line with vortex centres. A similar behaviour is observed for the production of the Reynolds shear stress. As also observed by Yoshioka et al. (2001a), the maxima are a consequence of the increased rate of strain between vortices generating turbulence. Conversely, the level of strain is relatively low within the vortices, thus resulting in a diminution of the generation rate. As regards the pressure–strain of the shear stress, absolute maxima are observed in the cores of the vortices, due to the large pressure fluctuations therein (the rather noisy behaviour is again due to the small sample size in the phase-averaged quantities).

The phase-averaged budgets of the Reynolds shear stress at the position $x/h = 2$ for two phase locations are presented in Fig. 16. The dissipation rate is seen to be small. While this is in line with expectations on physical grounds, this quantity must be regarded as unreliable, because of its association with the smallest scales in the flow. Despite the rather noisy appearance of the distributions, the imbalance is smaller than 5% of the peak production. The budgets are clearly dominated by the production and the pressure–strain process, and this is similar to the behaviour observed in steady flow. However, the relative levels of these two principal contributions vary significantly in time. The line $x/h = 2$ at $\phi = 0$ traverses a vortex centre, and this is characterized, as noted earlier, by a low rate of production and high pressure–strain level. In contrast, the line traverses the flow between two vortices at $\phi = \pi$, in which case production is high and pressure–strain low.

Computed phase-averaged velocity and turbulence-energy profiles at two streamwise locations are shown in Fig. 17. Both sets of velocity profiles feature significant variations in the strain rate within the shear layer during the period of injection. The effect on the turbulence-energy profiles is less clear, however. Although there is, at $x/h = 2$, some degree of correlation between the shear strain and the level of turbulence energy, this correspondence is lost at $x/h = 4$. Indeed, at this location, the level of turbulence energy is rather insensitive to the

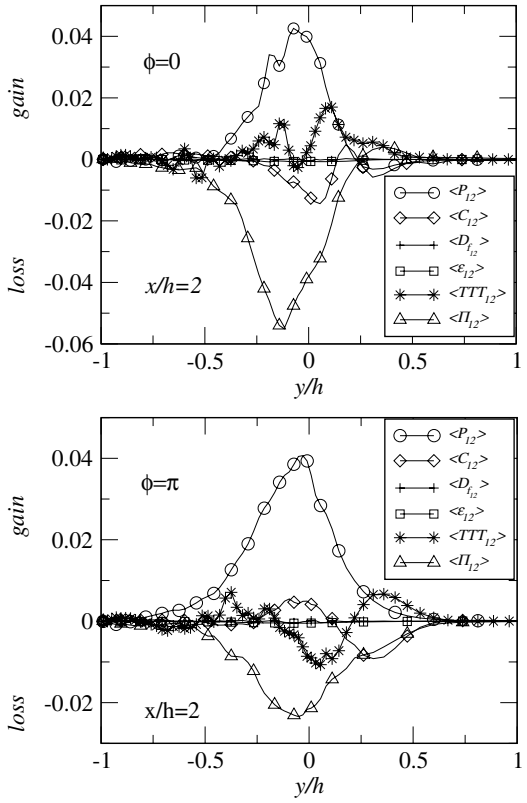

Fig. 16. Phase-averaged budget of the Reynolds shear stress $-\langle uv\rangle/U_c^2$ at the location $x/h = 2$; production $\langle P_{12}\rangle$; convection $\langle C_{12}\rangle$; viscous diffusion $\langle D_{f_{12}}\rangle$; dissipation $\langle \varepsilon_{12}\rangle$; turbulent transport $\langle TTT_{12}\rangle$; pressure–strain Π_{12}. All the budget terms (see Eq. (5)) are normalized by U_c^3/h.

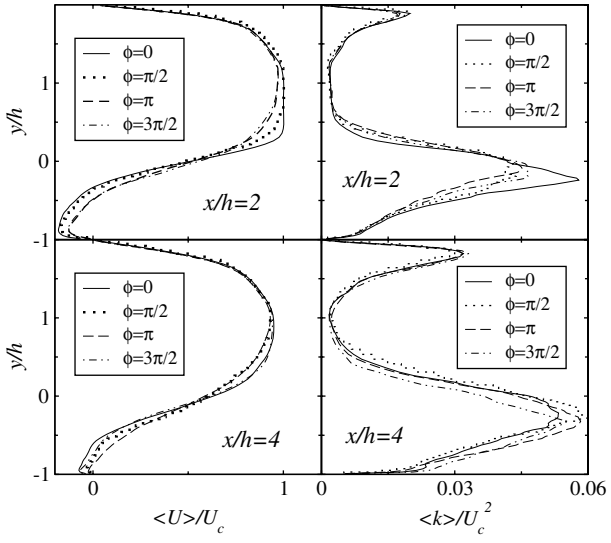

Fig. 17. Phase-averaged streamwise velocity and turbulence energy downstream the step at the locations $x/h = 2$ and $x/h = 4$.

changes in the phase-averaged strain, remaining almost constant. As this level has been observed to be close to that of the time-averaged turbulence energy (Fig. 8 gives the streamwise and cross-stream component only at $x/x_{r,o} = 0.72$, corresponding to $x/h = 4$), it follows that the direct contribution of the phase-averaged motion, associated with the large-scale structures seen in Fig. 12, to the time-averaged turbulence energy must be small at this location and beyond. Hence, it appears that the substantial elevation of the time-averaged turbulence level at $x/x_{r,o} = 0.72$, seen in Fig. 8, reflects transport from usptream in combination with local amplification of turbulence due to the interaction of the perturbation with the shear-layer instability.

5.4. Spectral analysis

Spectral analysis may be used to shed light on why a particular perturbation frequency leads to a preferential response of the perturbed baseline flow. In the present case, that frequency corresponds to $St = 0.2$, a value for which a maximum reduction in the recirculation length results. As noted in Section 1, previous spectral studies of separated flow suggest the existence of two types of instability: the shear-layer mode and the shedding-type mode. In experiments pertaining to the control of a flow over a backward-facing step, Bhattacharjee et al. (1986), Hasan (1992) and Chun and Sung (1996) have found that the most effective forcing frequency, scaled on the momentum thickness of the shear layer, θ, is comparable to the frequency of the unforced shear-layer-instability mode, $St_\theta = f\theta/U_c \sim 0.1$. The present results support this finding. This emerges from the frequency spectrum of the streamwise velocity fluctuation given in Fig. 18(a) for the unforced flow downstream of the step in the shear-layer at the location $x/h = 3$, $y/h = 0$. The spectrum features a peak located at the frequency $St = 0.2$.

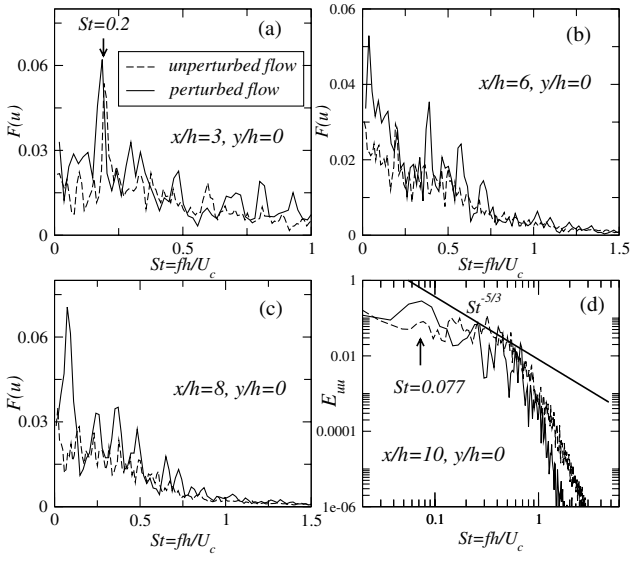

Fig. 18. Unperturbed and perturbed flows: frequency spectra at different streamwise locations downstream the step.

This is the frequency to which the flow is observed experimentally to be most receptive. Normalized by the local momentum thickness, θ, this frequency takes the value $St_\theta = 0.096$, which is close to the experimentally observed value for the shear-layer-instability mode. The frequency spectrum of the forced flow also exhibits a peak at $St = 0.2$, but due to the periodic perturbation, the peak is amplified compared to the unforced flow.

As pointed out already, an important mechanism affecting the reattachment process is the formation of large vortical structures in the shear layer, which interact with the wall. These are associated with the low-frequency 'flapping' motion of the shear layer, also referred to as the shedding-type instability (Sigurdson, 1995, Kiya et al., 1997). This motion, which reflects the interaction of the entire shear layer with the wall, applies to both the unforced and the forced flow. It is found to be characterized by the frequency $St \sim fh/U_c \sim 0.08$ in various flow geometries. Because of the large scales associated with this low-frequency mode, it manifests itself well downstream of the reattachment region. Fig. 18(a)–(c) shows the spectrum of the streamwise velocity fluctuations along the shear-layer at $x/h = 3, 6$ and 8, for both the unperturbed and perturbed flows. As the flow progresses from the separation point, the frequency corresponding to the energy peak shifts towards lower values, reflecting the growth by diffusion or pairing of the initial vortical structures that emerge from the step and are convected downstream. Further downstream, at $x/h = 10$, the energy-density spectrum of the streamwise velocity fluctuations (Fig. 18(d)) exhibits, for both flow conditions, a low-frequency peak at $St = 0.077$, a value which agrees well with the above-noted experimental studies. This peak is directly related to the periodic behaviour of the reattachment (see Fig. 14), which is induced by the passage of the large-scale structures impinging upon the wall. The comparison of the spectra for the perturbed and unperturbed flows has not given evidence of a fundamental change in the structure of the flow. However, as a direct result of the injection, the amplitude of the spectra is higher when the flow is perturbed.

6. Conclusions

The simulations may be claimed to have reproduced all major experimentally observed features of the response of the present backward-facing-step flow to the perturbation provoked by an unsteady jet injected into the separating shear layer.

At a global level, the computation correctly predicted the substantial reduction in the size of the recirculation zone – around 30% relative to the length in the unperturbed flow. This reduction was found to be associated with a correspondingly large increase in the time-averaged turbulence intensity normal to the shear layer and in the shear stress within the layer.

A consideration of the phase-averaged characteristics revealed that the increase in the time-averaged Reynolds stresses reflects, primarily, the generation of large vortical structures in the recirculation region below the shear-layer. These large structures interact strongly with the wall, a process that induces a 'flapping' motion of the whole shear-layer, referred to as *shedding-type instability*. The large structures travel downstream with a characteristic convective speed of about 40% of the velocity of the main stream prior to separation, and the passage of these vortical structures causes large fluctuations in the reattachment line. One effect of the large vortical structures is the increased generation of phase-averaged turbulence energy in regions between the structures due to additional strain. However, this effect becomes weak as the flow progresses towards and beyond the reattachment location. Here, the elevation of turbulence activity in the perturbed flow is due to transport from upstream regions in combination with local amplification of turbulence as a results of the interaction between the perturbation and the shear layer instability.

The simulation has provided evidence, supported by an examination of spectra, that the strong sensitivity of the flow to the forcing at the optimal Strouhal number, $St = 0.2$, is due to the perturbation causing specific changes to the evolution of the vortical structures within the separated shear layer. The perturbation is in 'tune' with the characteristic timescale associated with vortex generation within the shear layer. This leads to an amplification of the forcing, which then enhances the flapping motion of the shear layer as a whole. Because the prediction of this interaction requires the resolution of the structures within the shear layer, RANS computations are unlikely to reproduce well the sensitivity observed herein. Indeed, comparisons reported in Jakarlić et al., 2001 show that RANS computations return only a modest reduction in the length of the recirculation region, because the unsteadiness in the shear layer is simply a consequence of a direct link to the unsteady jet-injection process.

Acknowledgements

The authors gratefully acknowledge the provision of experimental data by Prof. S. Obi and Dr. S. Yoshioka, additional to those published in Yoshioka et al. (2001a,b). The authors are also grateful for the financial support provided by the UK Engineering and Physical Sciences Research Council (EPSRC) and by BAE Systems. The simulations were performed on the Cray T3E computer of the national CSAR service at the

University of Manchester with an allocation provided to the authors by EPSRC.

References

Akselvoll, K., Moin, P., 1995. Large eddy simulation of turbulent confined coanular jets and flow over a backward-facing step. Thermosciences Division, Department of Mechanical Engineering, Rept. TF-63, Stanford University, Stanford, CA.

Armali, B.F., Durst, F., Pereira, J.C.F., Schönung, B., 1983. Experimental and therotical investigation of backward-facing step flow. Journal of Fluid Mechanics 127, 473–496.

Bhattacharjee, S., Scheelke, B., Troutt, T.R., 1986. Modification of vortex interactions in a reattaching separated flow. AIAA Journal 24 (4), 623–629.

Chun, K.B., Sung, H.J., 1996. Control of turbulent separated flow over a backward-facing step by local forcing. Experiments in Fluids 21, 417–426.

Chun, K.B., Sung, H.J., 1998. Visualisation of a locally-forced separated flow over a backward-facing step. Experiments in Fluids 25, 133–142.

Ducros, F., Nicoud, F., Poinsot, T., 1998. Wall-adapting local eddy-viscosity models for simulation in complex geometries. In: 6th ICFD Conference on Numerical Methods for Fluid Dynamics, pp. 293–299.

Hasan, M.A.Z., 1992. The flow over a backward-facing step under controlled perturbation: laminar separation. Journal of Fluid Mechanics 238, 73–96.

Jakarlić, S., Jester-Zürker, R., Tropea, C., 2001. Proc. 9th ERCOFTAC/IAHR/COST Workshop on refined turbulence modelling.

Kasagi, N., Matsunaga, A., 1995. Three-dimensional particle-tracking velocimetry measurement of turbulence statistics and energy budget in a backward-facing step flow. International Journal of Fluid and Heat Flow 16, 477–485.

Kiya, M., Shimizu, M., Mochizuki, O., 1997. Sinusoidal forcing of a turbulent separation bubble. Journal of Fluid Mechanics 342, 119–139.

Lardat, R., Leschziner, M.A., 1998. A Navier–Stokes solver for LES on parallel computers. Technical Report, Department of Mechanical Engineering, UMIST.

Le, H., Moin, P., Kim, J., 1997. Direct numerical simulation of turbulent flow over a backward-facing step flow. Journal of Fluid Mechanics 330, 349–374.

Parneix, S., Laurence, D., Durbin, P.A., 1998. A procedure for using DNS data. ASME 120, 40–47.

Schumann, U., Sweet, R.A., 1988. Fast Fourier transforms for direct solution of Poisson's equation with staggered boundary conditions. Journal of Computational Physics 75, 123–137.

Sigurdson, L.W., 1995. The structure and control of a turbulent reattaching flow. Journal of Fluid Mechanics 298, 139–165.

Temmerman, L., Leschziner, M.A., Mellen, C.P., Fröhlich, J., 2003. Investigation of wall-function approximations and subgrid-scale models in large eddy simulation of separated flow in a channel with streamwise periodic constrictions. International Journal of Heat and Fluid Flow 24, 157–180.

Wengle, H., Huppertz, A., Bärwolff, G., Janke, G., 2001. The manipulated transitional backward-facing step flow: an experimental and direct numerical investigation. European Journal of Mechanics B—Fluids 20, 25–46.

Yoshioka, S., Obi, S., Masuda, S., 2001a. Organized vortex motion in periodically perturbed turbulent separated flow over a backward-facing step. International Journal of Heat and Fluid Flow 22, 301–307.

Yoshioka, S., Obi, S., Masuda, S., 2001b. Turbulence statistics of periodically perturbed separated flow over a backward-facing step. International Journal of Heat and Fluid Flow 22, 393–401.